In-Situ FTIR Study of CO_2 Adsorption and Methanation Mechanism Over Bimetallic Catalyst at Low Temperature

Daxin qin[1] · Dengbing Xie[1] · Heping Zheng[2] · Zhongwei Li[1] · Jianhua Tang[1] · Zhengjun Wei[2]

Abstract

Ni-based catalysts are the most promising catalysts for CO_2 methanation. The development of catalysts with low-temperature activity could bring significant energy and environmental benefits. In this work, the hydrogenation of CO_2 to methane was studied on Ni-M/γ-Al_2O_3 (M = Fe, Co, or Mn) bimetallic catalysts. The optimum reaction was obtained using Ni-Mn/γ-Al_2O_3 (CO_2 conversion: 85%, CH_4 selectivity: 99%, 280 °C). In situ FTIR studies revealed the excellent performance of Ni-Mn/γ-Al_2O_3, which lowers the required reaction temperature. Based on in situ FTIR studies, CO_2 methanation proceeded over three intermediates on the catalysts: bicarbonate → carbonate → formate → methane. The second metal (Co or Mn) promoted the dispersion of both Ni and itself and improved the ability of Ni to crack H_2. And introduced more oxygen vacancies to strengthen the basicity of surrounding O^{2-} on the surface of the catalysts. In effect, the number of carbonate active sites could be increased accordingly, thereby improving the adsorption capacity for CO_2.

Graphic Abstract
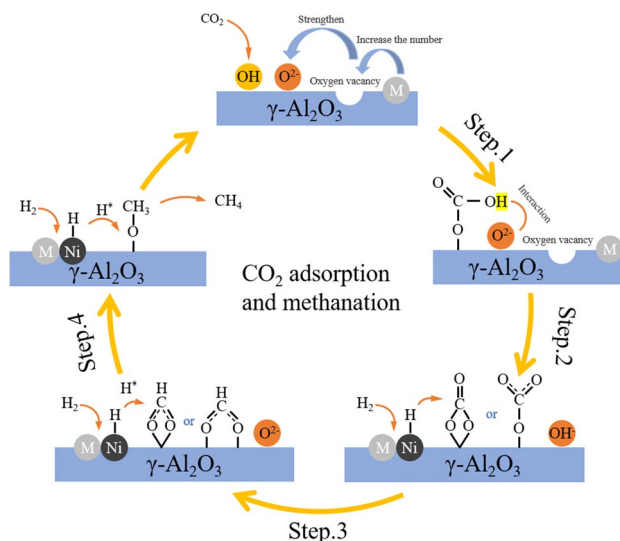
✉ Jianhua Tang
tangjianhua@scu.edu.cn

1 College of Chemical Engineering, Sichuan University, Chengdu 610065, People's Republic of China

2 Sichuan Coal Industry Group Limited Liability Company, Chengdu 610091, People's Republic of China

1 Introduction

Global warming is one of the most important environmental issues in the twenty-first century. Limiting excessive production of CO_2 is of great practical significance to delay global warming. CO_2 methanation technology

is considered to be one of the most effective technologies for CO$_2$ recycling [1], and the main reaction is: CO$_2$ (g) + 4H$_2$ (g) → CH$_4$ (g) + 2H$_2$O (g); $\Delta H_{298K} = -165$ kJ/mol, $\Delta G_{298K} = -114$ kJ/mol, which is known as the Sabatier reaction [2]. As this reaction is exothermic, a lower temperature is conducive for the conversion of CO$_2$. Most of the products are CH$_4$ and H$_2$O at 200–250 °C, but the yield and selectivity for CH$_4$ decrease as the temperature increases [3, 4]. Moreover, CO$_2$ is chemically stable and difficult to convert. Hence, the catalyst used for CO$_2$ methanation needs to exhibit relatively high activity.

The active components of methanation catalysts are usually Ni, Fe, Co, Ru, and Rh [5–11]. Among which, Ni is widely used as a research object because of its high activity, selectivity for CH$_4$, and low cost. However, it is difficult for Ni catalysts to achieve high CO$_2$ conversion at low temperatures due to high thermodynamic barriers. Utilizing a second metal to form bimetallic catalysts is an effective way to lower the required reaction temperature, but the candidates for such metals are dominated by precious metals such as Pd, Ru, and Pt [7, 12, 13]. Therefore, it is necessary to investigate low-cost additives. Part of the previous research suggested that transition metals, such as Fe, Co, and Mn [14–19], may form a close interaction with Ni after annealing, thereby lowering the reduction temperature and increasing the dispersion of Ni. Density functional theory calculations have also suggested that the addition of these second metals can reduce the activation energy of CO$_2$ methanation [20]. The chemical state of highly dispersed Ni on the surface of the support may play a key role in CO$_2$ methanation, which means that surface species on supports must be identified for further understanding.

In situ Fourier transform infrared (in situ FTIR) spectroscopy is a powerful characterisation method that can be used to investigate CO$_2$ adsorption, desorption, and reaction process intermediates over a catalyst surface. Although many studies have investigated CO$_2$ methanation on Ni-, Ru- and Rh-based catalysts by in situ FTIR [21–25], there is no unified view among the research on the reaction mechanism. Dreyer et al. [21] suggested that the first step of CO$_2$ methanation is the dissociation of CO$_2$. CO$_2$ gradually dissociates into CO, C* and O* in the presence of a catalyst and then forms hydroxymethylene (HCOH) with the assistance of H*, finally was abstracted by O to form CH$_4$. Marwood et al. [25] proposed that CO$_2$ is first adsorbed on the support in the form of bicarbonate and then reacts with spilled over H* cracked by an active component to form formate intermediates on the metal surface. Finally, formate reacts with H*, which then leads to methanation. However, there is minimal comprehensive research on in situ FTIR measurements for the mechanism of CO$_2$ methanation by the addition of second metals. Moreover,

it is still a challenge to develop low-cost catalysts with high activity at low temperatures (< 300 °C) [26].

In this study, we reported the effects of bimetallic catalysts Ni-M/γ-Al$_2$O$_3$ (M = Fe, Co, or Mn) for CO$_2$ methanation, and the results showed that the addition of second metal Mn or Co significantly enhanced the catalytic performance of Ni/-Al$_2$O$_3$. Various characterization methods including XRD, SEM-EDS, XPS, H$_2$-TPR and CO$_2$-TPD were performed to demonstrate the changes in physicochemical properties. CO$_2$ adsorption and methanation intermediate identification was performed via in situ FTIR, and the mechanism of CO$_2$ adsorption and methanation was further analysed.

2 Material and Methods

2.1 Catalysts Preparation

Bimetallic catalysts were prepared via an ultrasonic assisted co-impregnation method using Ni(NO$_3$)$_2$·6H$_2$O and Fe(NO$_3$)$_3$·9H$_2$O, Co(NO$_3$)$_2$·6H$_2$O, or Mn(NO$_3$)$_2$ (50%) for the addition of the second metal. First, γ-Al$_2$O$_3$ (40–60 mesh) was impregnated in a mixed aqueous solution of appropriate concentrations of nickel nitrate and the nitrate salt of the second metal; the solution was then sonicated for 20 min using an ultrasonic oscillator. Then, the samples were naturally dried at 25 °C for 12 h and then at 120 °C for 2 h. The prepared precursor was annealed under a N$_2$ flow (200 mL/min) at 850 °C (the temperature was raised from room temperature to 850 °C at a rate of 10 °C/min) for 4 h and reduced under a 10% H$_2$-N$_2$ flow (200 mL/min) at 850 °C for 4 h. Finally, a bimetallic catalyst with a Ni load of 10wt% and a second metal load of 2.5wt% was obtained, denoted as Ni-M/ γ-Al$_2$O$_3$ (M = Fe, Co, or Mn).

2.2 Catalytic Tests

Catalytic tests were performed in a tubular fixed-bed flow reactor with an inner diameter of 10 mm under atmospheric pressure. First, 500 mg of the catalyst sample mixed with 2.5 g of SiC (40–60 mesh) dilution was loaded into the reactor, and a flow of H$_2$ and CO$_2$ (H$_2$/CO$_2$ = 4) mixture at 100 ml/min (12,000 mL/h·gcat) was passed through the catalyst bed. The tests were carried out at 160–380 °C in steps of 20 °C that were maintained for 30 min each to achieve a stable condition and measure three times to take the average. The effluent gases composition was monitored with a gas chromatograph (Agilent 8890). The CO$_2$ conversion and CH$_4$ selectivity were calculated using the equations below.

$$X_{CO_2} = \frac{F_{in} \times C_{CO_2,in} - F_{out} \times C_{CO_2,out}}{F_{in} \times C_{CO_2,in}} \times 100\% \tag{1}$$

$$S_{CH_4} = \frac{C_{CH_4,out}}{C_{CH_4,out} + C_{CO_2,out}} \times 100\% \qquad (2)$$

The thermodynamic equilibrium calculations were derived from the mathematical model R-Gibbs in Aspen Plus software. Only CH_4 and CO were detected as carbonaceous products in the reactor outlet stream.

2.3 Characterization

The phases composition of all samples were determined by powder X-ray diffraction (XRD) on an X'Pert-ProMPD diffractometer using Cu Kα radiation (λ = 1.54 Å) at an angle of 10°–80° at 40 kV and 30 mA, and the scanning step was 0.02°/s.

The catalyst particles were ground to obtain powders needed for energy-dispersive spectroscopy (EDS) mapping using a scanning electron microscopy (SEM) instrument.

The temperature-programmed reduction (H_2-TPR) test was performed using an AutoChem II 2920 instrument equipped with a TCD. A 500-mg sample was loaded and investigated under a 5% H_2/N_2 flow (30 mL/min) at 50–1000 °C with a temperature ramping rate of 10 °C/min.

The elemental composition and valence of all samples were determined by X-ray photoelectron spectra (XPS) on a AXI Sultra DLD Spectrometer employing a monochromatized Al-Kα X-ray source (hν = 1486.6 eV), and all binding energies were referenced to the C 1 s at 284.8 eV.

The temperature-programmed desorption (TPD) of CO2 was also performed using an AutoChem II 2920 instrument equipped with a TCD. Before TPD measurements, the catalyst was pre-treated under He flow at 450 °C for 90 min and cooled to 50 °C. A flow of 20% CO_2/He mixture at 30 mL/min pass through the sample for 1 h and the weakened

physical adsorption of CO_2 was removed by a He flow at 30 mL/min for 1 h. Finally, the temperature is increasing to 700 °C at a rate of 10 °C /min.

2.4 In Situ FTIR Measurements

In situ FTIR measurements were performed using a Thermo Nicolet iS50 spectrometer equipped with a reaction cell with CaF_2 windows. Four scans were averaged for each spectrum, which were recorded at a resolution of 4 cm^{-1}. After the powders were pressed, 30 mg of the catalyst powder was loaded into the cell for vacuum pre-treatment at 450 °C for 90 min. For CO_2 adsorption measurements, an amount of CO_2 was fed into the in situ FTIR cell at 60 °C, with scanning every 30 s. For CO_2 methanation intermediate measurements, a flow of H_2 and CO_2 ($H_2/CO_2 = 4$) mixture with a total flow rate of 50 mL/min was fed into the in situ FTIR cell. The reaction was performed at 60–300 °C (ramping rate of 10 °C/min) with scanning every 2 min.

3 Results and Discussion

3.1 Catalytic Test

Figure 1 shows the CO_2 methanation performance of Ni/γ-Al_2O_3 and Ni-M/γ-Al_2O_3 catalysts. As shown in Fig. 1a, the T_{50} values, corresponding to the temperature at 50% conversion, are 269, 275, 220, and 232 °C for Ni/γ-Al_2O_3, Ni-Fe/γ-Al_2O_3, Ni-Mn/γ-Al_2O_3, and Ni-Co/γ-Al_2O_3 respectively. In addition, in the presence of Ni-Mn/γ-Al_2O_3, the highest CO_2 conversion of 85% was measured at 280 °C; similarly, the corresponding value for Ni-Co/γ-Al_2O_3 of 84% was measured at 300 °C. This result clearly indicates a significantly enhanced low-temperature activity for CO_2 methanation
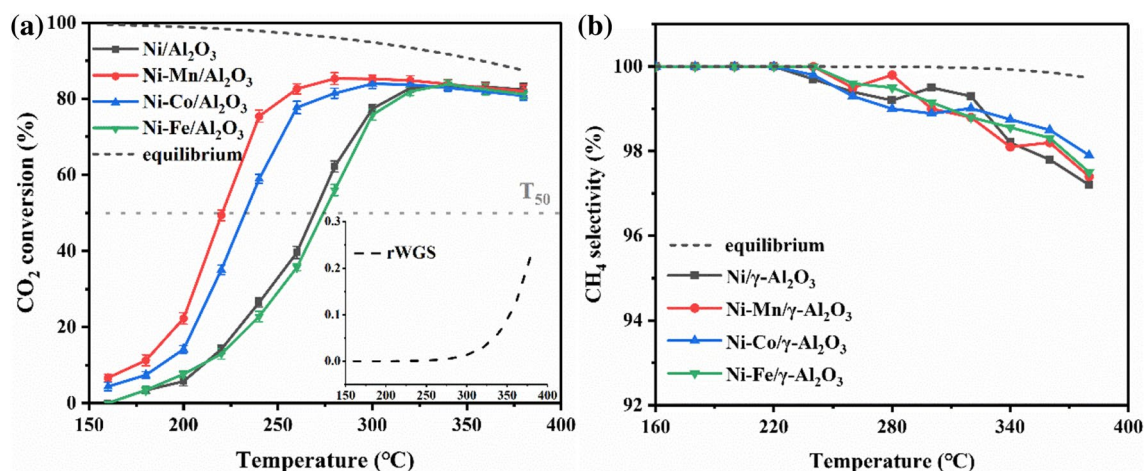

Fig. 1 Catalytic active tests. **a** CO_2 conversion and **b** CH_4 selectivity

compared with that of Ni/γ-Al$_2$O$_3$, which yielded its highest conversion rate of 83% at 340 °C. Because Ni-Fe/γ-Al$_2$O$_3$ yielded its highest conversion rate of 84% at 340 °C, this catalyst did not exhibit a significant improvement in conversion rate and low-temperature activity compared to Ni/γ-Al$_2$O$_3$. For temperatures higher than 380 ℃ the reaction is close to thermodynamic equilibrium for all catalysts, and the approach to equilibrium at conversions higher than 80% slows down while the thermodynamic equilibrium of the reverse water gas reaction is very low, therefore, it is mainly that the product gas, especially H$_2$O, inhibits the conversion of CO$_2$ to approach thermodynamic equilibrium [27]. Figure 1b shows the CH$_4$ selectivity as a function of reaction temperature. The Ni catalyst alone exhibited high CH$_4$ selectivity, with CH$_4$ selectivity of over 96% at reaction temperatures below 400 °C. The addition of the second metal did not significantly improve the CH$_4$ selectivity at the same reaction temperatures. However, due to the reduction of the optimum reaction temperature when using Ni-Mn/γ-Al$_2$O$_3$ and Ni-Co/γ-Al$_2$O$_3$ catalysts, the corresponding CH$_4$ selectivity was also slightly improved.

3.2 Catalyst Characterization

Figure 2 shows the results of XRD measurements. From Fig. 1a, for the annealed catalyst precursor, the diffraction peaks are assigned to NiAl$_2$O$_4$ (JCPDS 73-0239) phases with shoulders that are attributed to γ-Al$_2$O$_3$ (JCPDS 10-04025) species. No obvious diffraction peaks for NiO specie can be detected, suggesting that the NiO is highly dispersed, incorporated into the structure of γ-Al$_2$O$_3$ support at high annealing temperatures. After reduction, the peaks of NiAl$_2$O$_4$ specie could hardly be observed, suggesting that NiAl$_2$O$_4$ has been completely reduced, and a series

diffraction peaks of Ni were observed. Figure 2b exhibit the XRD patterns of Ni-M/γ-Al$_2$O$_3$ after reduction. The reflections of Ni at $2\theta = 44.5°$ (1 1 1), 51.85° (2 0 0) and 75.38° (2 2 0) that were slightly broader and weaker in intensity compared with them of Ni/γ-Al$_2$O$_3$, suggesting a reduction in Ni particle size upon adding Mn, Fe, or Co. Burger et al. [28–30] suggested that the reduction of Fe or Co interacts with metallic Ni phase, leading to Ni lattice distortion by the formation of a Ni–Fe alloy. The formation of Ni–Fe alloy would shift the peak at 44.5°, 51.85° and 75.38° of metallic Ni phase towards a low angle, although this change was not obvious. Mn species might be incorporated into the former NiO-rich matrix or that the Mn species are modified under reduction conditions, leading to a change of the lattice constant of the former mixed oxide phase, and it appears in the XRD pattern as peaks at $2\theta = 36.4°$ and 65.0° shift to lower diffraction angles [28]. We calculated the crystal size of Ni using the Scherer formula, the average particle size of Ni in Ni/γ-Al$_2$O$_3$ is 14.3 nm, while in Ni-Mn/γ-Al$_2$O$_3$, Ni-Co/γ-Al$_2$O$_3$ and Ni-Fe/γ-Al$_2$O$_3$ are 11.3 nm, 11.8 nm, 12.0 nm, respectively. Combining with the conversions results, the introduction of Co or Mn could reduce the crystal size of Ni, which is beneficial to CO$_2$ methanation, but Fe has little effect. Therefore, we suggest that the size and dispersion of Ni are not the main reasons that affect CO$_2$ methanation in bimetallic catalysts. The absence of reflections assigned to Mn, Fe, and Co is likely due to they were well dispersed or the amounts of them are under the detection limit of XRD analysis.

To further verify that Mn, Fe, and Co were successfully loaded onto the surface of Ni/γ-Al$_2$O$_3$, we ground the catalyst samples into powders. Figure 3 shows the SEM-EDS mapping to obtain images of the elemental distribution on the surfaces of the Ni-M/γ-Al$_2$O$_3$ (M = Mn, Fe, or Co)
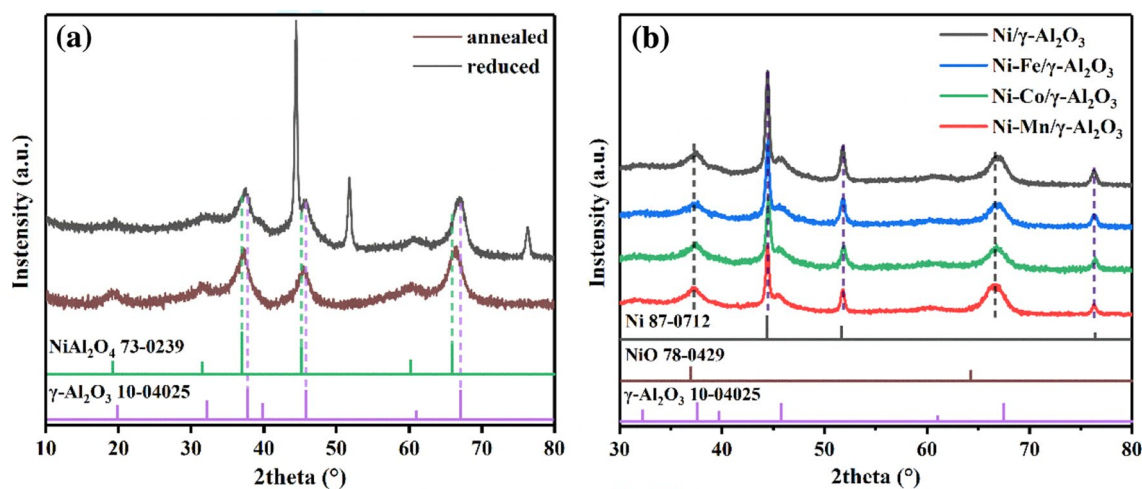

Fig. 2 XRD patterns of the Ni/γ-Al$_2$O$_3$ catalysts annealed at 850 °C and reduced at 850 °C (**a**) and Ni-M/γ-Al$_2$O$_3$ catalysts reduced at 850 °C (**b**)
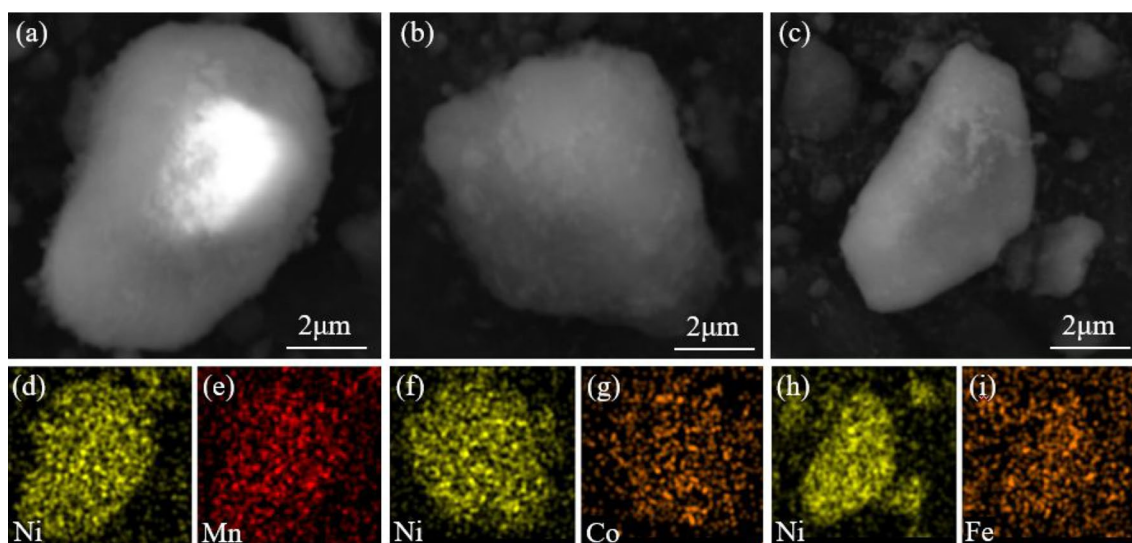
Fig. 3 SEM image of Ni-M/γ-Al$_2$O$_3$, M = Mn (**a**), M = Fe (**b**), M = Co (**c**), and EDS mapping images of each catalyst (**d–i**)
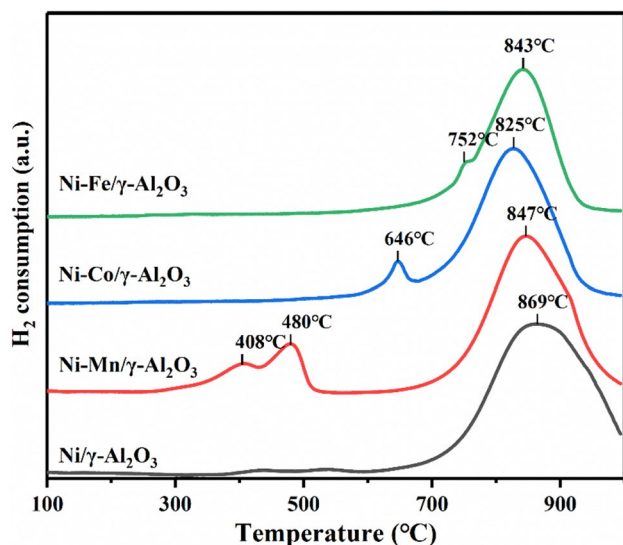

Fig. 4 H$_2$-TPR profiles of as-prepared Ni/γ-Al$_2$O$_3$ and Ni-M/γ-Al$_2$O$_3$ (M = Co, Fe, or Mn)

catalysts. The results indicate that Mn, Fe, and Co were uniformly incorporated and well dispersed on the supports with Ni, which is consistent with the XRD results.

In order to distinguish the states of the Ni^{2+} species and investigate the interactions between Ni/γ-Al$_2$O$_3$ and Ni-M/γ-Al$_2$O$_3$ before reduction, H$_2$-TPR characterisation was carried out, and the results are shown in Fig. 4. No other peaks were detected at 100–600 °C, indicating that no NiO species was generated. The strong peaks located at 800–1000 °C can be attributed to the presence of NiAl$_2$O$_4$ spinel. NiAl$_2$O$_4$ spinel was extremely difficult to reduce,

but Ni was more evenly dispersed after reduction because of the strong interaction between Ni and γ-Al$_2$O$_3$.

The addition of Mn, Co, and Fe to Ni/γ-Al$_2$O$_3$ led to different hydrogen consumption features, such as the peaks corresponding to the reduction of MnO$_2$ to Mn$_3$O$_4$ at 408 °C and the subsequent reduction to MnO at 480 °C; such peaks appear approximately 30 °C higher than those of bulk Mn on γ-Al$_2$O$_3$ [31]. The signals at 646 °C and 752 °C can be attributed to CoO and FeO, respectively, and it can be observed that the addition of different second metals lowers the reduction temperature of NiAl$_2$O$_4$ to different degrees. This result, in combination with the results of the XRD characterisation, indicates that the second metal oxide interacts with NiAl$_2$O$_4$ in ways that are beneficial to the dispersion of Ni.

To further understand the surface composition and valance state of these catalysts, X-ray photoelectron spectroscopy (XPS) were performed over Ni-M/γ-Al$_2$O$_3$ catalysts (Fig. 5). Peaks at 852–854 eV (Fig. 5a) can be assigned as Ni 2p$_{3/2}$ XPS spectra corresponding to Ni^0 and Ni^{2+} [32], respectively, indicating that Ni species existed as metallic Ni and nickel oxide/hydroxide [33, 34]. The ratio of Ni^0 to Ni^T (Ni^T = Ni^0 + Ni^{2+}) in Ni 2p$_{3/2}$ calculated by the area integrals was shown in Table 2. The ratio of Ni^0 was increased with adding the second metal compared with Ni/γ-Al$_2$O$_3$, indicating that it could be easier for the oxidation state of the element Ni reducing to Ni due to the existence of Fe, Co or Mn, which was also consistent with the results obtained by H$_2$-TPR. The peak of Ni^0 in 2p$_{3/2}$ shifted from 851.7 to 850.9 eV on Ni-Mn/γ-Al$_2$O$_3$ catalyst can be attributed to the electronegative of Mn (1.55) is lower than it of Ni (1.91), and the electrons can be transferred easier from Mn to Ni, and the electronegative of Fe(1.80) or Co(1.88) is similar to it of Ni, so the peak
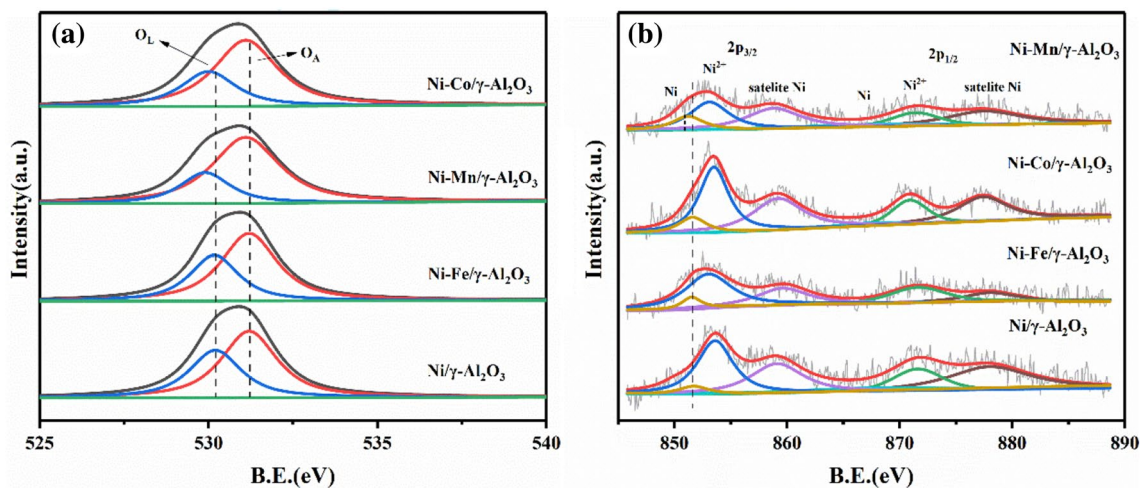
Fig. 5 Binding energy for elements of O 1s (**a**), Ni 2p (**b**) on Ni//γ-Al$_2$O$_3$ and Ni-M/γ-Al$_2$O$_3$ catalysts

Table 1 Summary of the XPS data for different catalysts

Catalyst	Ni^0/Ni^T/%	O$_L$/O$_T$/%
Ni/γ-Al$_2$O$_3$	7.3	39.1
Ni-Fe/γ-Al$_2$O$_3$	12.4	37.1
Ni-Mn/γ-Al$_2$O$_3$	28.1	25.7
Ni-Co/γ-Al$_2$O$_3$	18.2	31.2

position of Ni^0 in 2p$_{3/2}$ on Ni-Fe/γ-Al$_2$O$_3$ or Ni-Co/γ-Al$_2$O$_3$ did not change much compared with it on Ni//γ-Al$_2$O$_3$.

The O 1s spectra region for Ni/γ-Al$_2$O$_3$ and Ni-M/γ-Al$_2$O$_3$ were shown at Fig. 5b. The peaks at 529.6–530.3 eV can be attributed to the lattice oxygen (O$_L$) of the γ-Al$_2$O$_3$ support, while the signals at 531.0–531.2 eV can be assigned to the adsorbed oxygen surface or hydroxyl groups (O$_A$) [35, 36]. The calculation results of the ratio of O$_L$ to O$_T$ (O$_T$ = O$_L$ + O$_A$) was shown in Table 1. The percentage of lattice oxygen on Ni-Mn/γ-Al$_2$O$_3$ and Ni-Mn/γ-Al$_2$O$_3$ is approximately 13.4% and 7.9% decreased of that for Ni /γ-Al$_2$O$_3$ respectively, and the peak position of O$_L$ shifted lower binding energy from 530.2 to 529.8 eV in comparison to the Ni /γ-Al$_2$O$_3$. However, the peak position of O$_L$ and the ratio of O$_L$ to O$_T$ on Fe-Ni /γ-Al$_2$O$_3$ did not change much compared with Ni/γ-Al$_2$O$_3$. We suggested that the addition of the second metal of Mn and Co may have an interaction with Ni/γ-Al$_2$O$_3$ after annealing making it easier to deprive the O$_L$ of the supports surface during H$_2$ reduction increase, which providing more oxygen vacancy. Because of the existence of oxygen vacancies, it will attract the surrounding lattice oxygen, resulting in a decrease in the binding energy of lattice oxygen. The addition of Fe to Ni/γ-Al$_2$O$_3$ did not result in more oxygen vacancies due to its high reduction temperature and strong
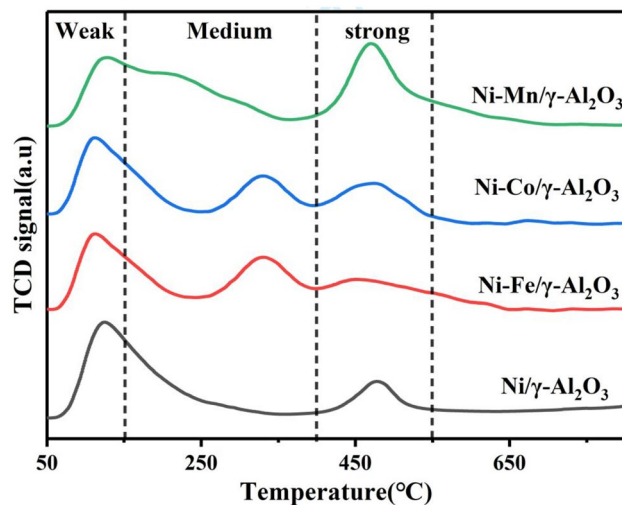

Fig. 6 CO_2 profiles of the Ni/γ-Al$_2$O$_3$ and Ni-M/γ-Al$_2$O$_3$ catalysts

interaction with γ-Al$_2$O$_3$, thus the catalytic performance of CO_2 methanation did not improve.

CO_2-TPD results for catalyst Ni-M/γ-Al$_2$O$_3$ are depicted in Fig. 6. Different basic sites correspond to different CO_2 desorption temperatures, so we divide the temperature of CO_2 desorption into three zones, CO_2 desorption between 50 and 150 °C exhibits weak basic sites, whereas desorption between 150 and 450 °C exhibits medium basic sites, and peaks signals between 450 and 550 °C is observed, originating from CO_2 desorbing from strong basic sites. In addition, we can find that Ni/γ-Al$_2$O$_3$ has almost no medium basic sites, but with the introduction of the second metal, the amount of medium basic sites on the catalyst increased significantly, especially the introduction of Mn, and the amount of strong basic sites also increased slightly. This indicates

that with adding the second metal, weakly basic sites may form medium basic or strong basic sites. Combining the conversion results, the introduction of Mn and Co increased the amounts of strong basic sites on the catalyst surface, thereby improving the activity of the catalyst, while the introduction of Fe causing opposite effect. The amounts of intermediate basic sites seemed also to affect the activity of the catalyst, otherwise, the conversion rate of CO_2 on Ni-Fe/γ-Al$_2$O$_3$ may be lower compared with it on /γ-Al$_2$O$_3$.

3.3 In Situ FTIR CO_2 Adsorption Measurements

To further understand the CO_2 adsorption species and reaction pathways, in situ FTIR CO_2 adsorption measurements were performed, and Table 2 presents a summary of the most commonly detected intermediates during CO_2 adsorption. The CO_2 adsorbed on γ-Al$_2$O$_3$ was mainly in the forms of bicarbonate and small amounts of monodentate and bidentate carbonate (Fig. 7a). The peaks at 1648, 1440, and 1228 cm^{-1} were attributed to bicarbonate; the weak peaks at 1554 and 1378 cm^{-1} were attributed to monodentate carbonate; the weak peaks at 1634 and 1350 cm^{-1} were assigned to bidentate carbonates [29]. The first step of CO_2 capture (Fig. 12, step 1) by –OH on γ-Al$_2$O$_3$ to form bicarbonate has already been described by other authors [39].

When Ni was loaded onto γ-Al$_2$O$_3$ for in situ FTIR CO_2 adsorption measurements (Fig. 7b), we observed that the peak for C–OH stretching of bicarbonate (1228 cm^{-1}) gradually weakened and the peak at 1648 cm^{-1} shifted to 1634 cm^{-1} with increasing adsorption time. Simultaneously, the O–C–O stretching signals of monodentate (1378 cm^{-1}) and bidentate carbonate (1350 cm^{-1}) slightly increased. Combined with the result of CO_2-TPD, bicarbonate, bidentate carbonate and monodentate carbonate can be considered as weakly basic sites, medium basic sites, and strong basic sites as described in CO_2-TPD results. It can thus be inferred that bicarbonate was transformed into carbonate. The assignment is in agreement with results of Ewald et al. [40].
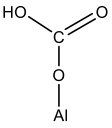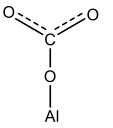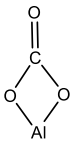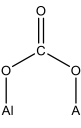
Figure 7c–e display the in situ FTIR spectra of CO_2 adsorption on Ni-M/γ-Al$_2$O$_3$ (M = Mn, Fe, or Co). The signals indicating the conversion of bicarbonate to carbonate were also observed. More interestingly, when the adsorption reached saturation (Fig. 6f), the addition of Mn, Fe or Co could provide more basic sites of monodentate and bidentate carbonate. In the case of Ni-Mn/γ-Al$_2$O$_3$ and Ni-Co/γ-Al$_2$O$_3$ in particular, the peak corresponding to O–C–O stretching of carbonate became sufficiently intense to almost completely overlap with the O–C–O stretching peak of bicarbonate and the signals of –OH of bicarbonate appear to have almost disappeared [27]. These results are almost the same as the results of CO_2-TPD, which are represented by the decrease in the amount of weakly basic sites and the increased in the amount of medium or strong basic sites. The catalyst reduced by NiAl$_2$O$_4$ spinel contained more oxygen vacancies compared reducing by NiO [41, 42], and we suggest that the oxygen vacancy on the subsurface trapped electrons from the surrounding Ni, Co, Fe or Mn atoms in the form of electron pairs [43, 44]. The electrons at the oxygen vacancies had a pulling effect on the electrons of the surrounding O^{2-}, which made O^{2-} strongly basic. Hence, bicarbonate could be converted to monodentate or bidentate carbonate, and its H would be abstracted by the strongly basic O^{2-} (Fig. 12, step 2). Combining these results with those from the H$_2$-TPR and XPS characterisations, the addition of second metal of Mn or Co might provide more oxygen vacancies, which strengthen the surrounding surface O^{2-} to form more strongly basic sites. When almost all of the CO_2 captured by –OH was converted to monodentate and bidentate carbonate through the abundant O^{2-} alkaline sites around –OH on the surface of the supports, the infrared signals of bicarbonate were difficult to observe. The addition Fe to Ni/γ-Al$_2$O$_3$ also yielded more strongly alkaline O^{2-} sites around the –OH groups on the surface of the support, but the amount was not as much as the addition of Mn and Co.

3.4 In Situ FTIR CO_2 Methanation Measurements

To further investigate the species formed on the catalyst surface during CO_2 methanation, as well as the reaction mechanism, we performed in situ FTIR CO_2 methanation measurements for each catalyst with temperature programming.

Table 2 Summary of experimentally detected IR bands during CO_2 adsorption [37, 38]

	Bicarbonate	Monodentate carbonate	Bidentate carbonate	Bridged carbonate
O–H	3610 ~ 3620			
ν_s(O–C–O)	1440 ~ 1450	1350 ~ 1420	1260 ~ 1350	1800 ~ 1870
ν_{as}(O–C–O)	1645 ~ 1670	1490 ~ 1560	1620 ~ 1680	1130 ~ 1280
δ(C–OH)	1220 ~ 1280			
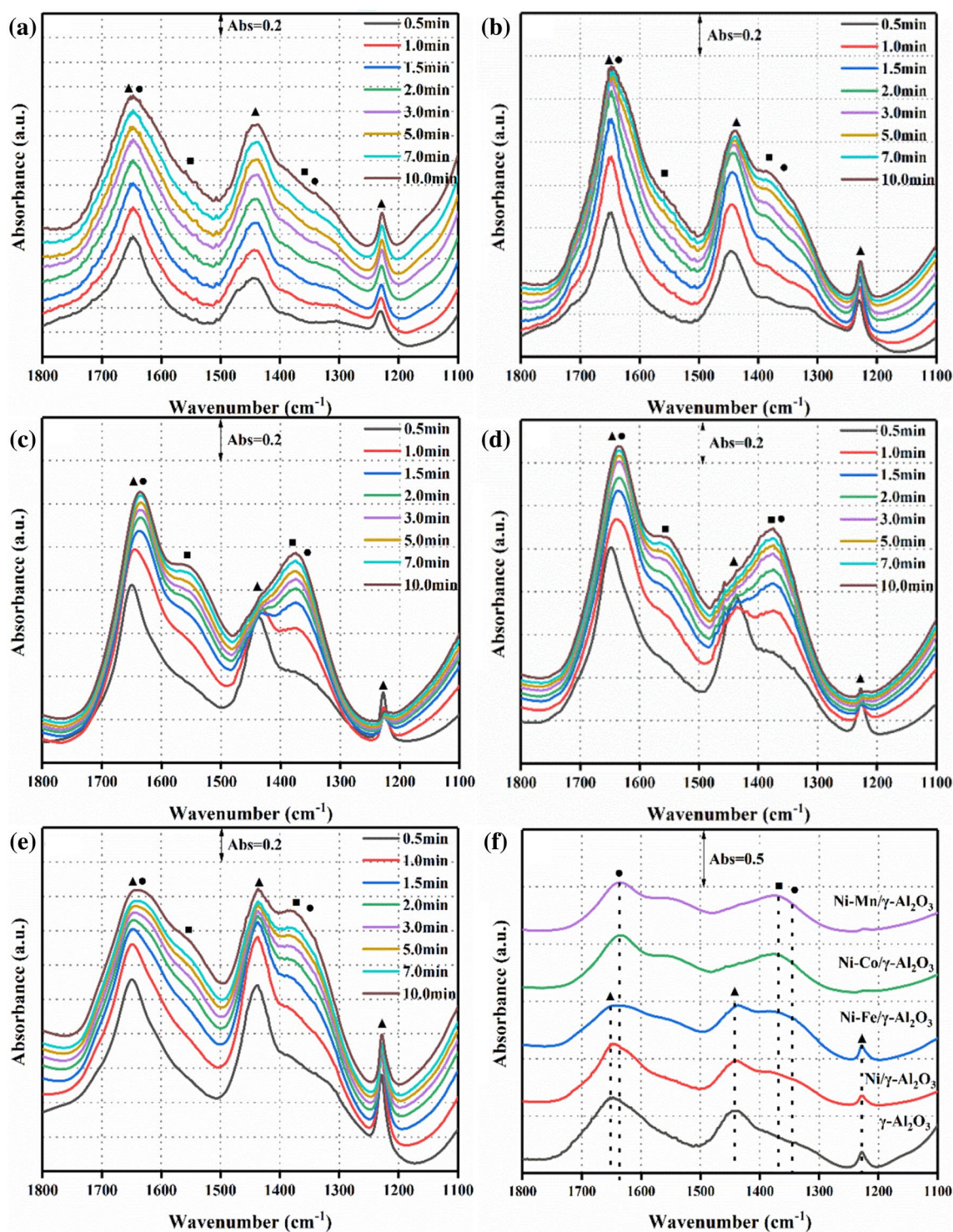
Fig. 7 In situ FTIR spectra of CO_2 adsorption on γ-Al_2O_3 (**a**), Ni/γ-Al_2O_3 (**b**), Ni-Mn/γ-Al_2O_3 (**c**), 10Ni-Co/γ-Al_2O_3 (**d**), and Ni-Fe/γ-Al_2O_3 (**e**) and saturated adsorption of each catalyst sample (**f**) (filled triangle bicarbonate, filled circle bidentate carbonate, filled square monodentate carbonate)

From 60 to 180 °C, it could be observed that the intensity of the peaks of bicarbonate and carbonate species adsorbed on the surface of Ni/γ-Al_2O_3 decreased as the temperature rose (Fig. 8). The peaks at 3700–3600 cm^{-1} could be attributed to CO_2 overtones [48], and the peaks at 3740–3640 cm^{-1} could be assigned to –OH groups of
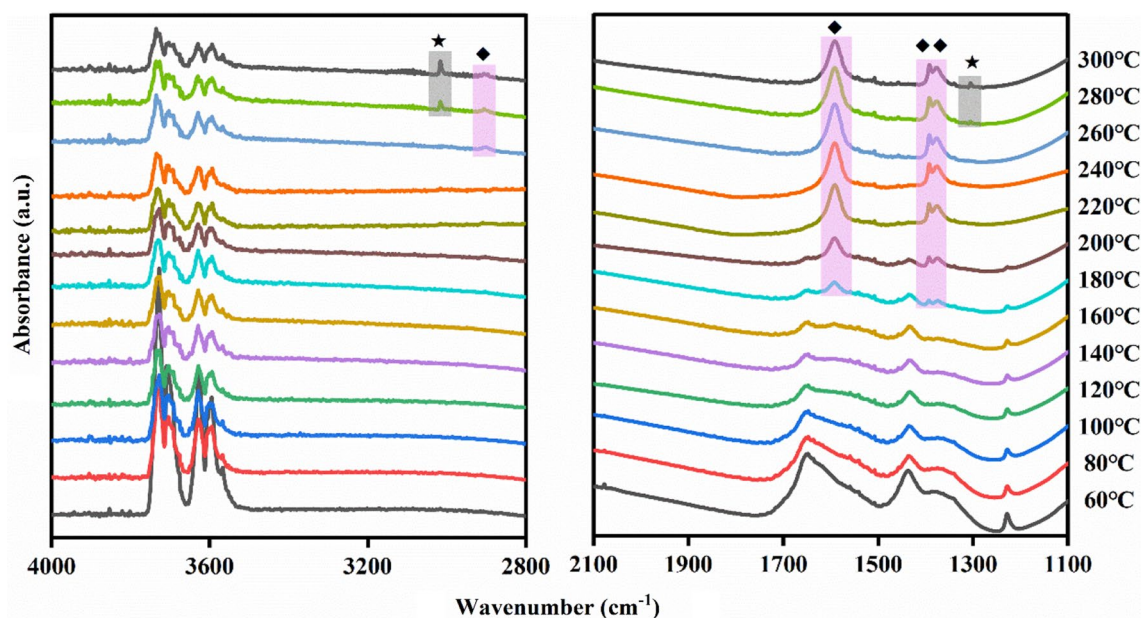
Fig. 8 In situ FTIR spectra of CO_2 methanation on Ni/γ-Al_2O_3 with a programmed temperature rise from 60 to 300 °C (filled diamond bidentate formate or bridged formate, filled star methane)

bicarbonates [21, 49]; the intensities of such peaks also weakened with CO_2 desorption. Starting at 180 °C, as the carbonate species became unstable with increasing temperature, the H cracked on the surface of Ni would be attracted by the carbon atoms on carbonates and then transferred to formate (Fig. 12, step 3). The peaks at 1590, 1370 ($\Delta v = 220$ cm^{-1}), and 1390 cm^{-1}, as well as the C–H peaks, could be attributed to monodentate and bridged formate (Table 3). When the temperature reached 260 °C, the appearance of C–H bands of formate at 2900 cm^{-1} was observed [50], and bands corresponding to C–H stretching of CH_4 appeared at 3016 cm^{-1} upon increasing the temperature by 20 °C. We suggest that the H* cracked by Ni spilled over onto the C atom and became unstable, which allowed us to observe peaks for the stretching vibration of C–H of monodentate and bridged formate. Subsequently, the

H atom bonded with the O atom to form H_2O, and hydro-dehydration followed by methanation occurred over several cycles (Fig. 12, step 4). During the whole process, we did not find the peak of Nickel carbonyl hydride at 1917 cm^{-1} or lineart CO on Ni at 2019 cm^{-1} so the formate did not transfer to the surface of metal Ni and the hydrogenation step may most occurred on the surface of the support.

Figures 9, 10 and 11 show in situ FTIR CO_2 methanation measurements of bimetallic catalysts Ni-M/γ-Al_2O_3 (M = Fe, Co, or Mn). The temperature at which point carbonate could be converted into formate was lowered to 100, 100, and 140 °C using Ni-Mn/γ-Al_2O_3, Ni-Co/γ-Al_2O_3, and Ni-Fe/γ-Al_2O_3, respectively. With the in situ FTIR CO_2 adsorption measurements, it was also suggested that a conversion relationship between carbonate and formate, as well as the introduction of the second metal,

Table 3 Summary of experimentally detected IR bands during CO_2 methanation [45–47]

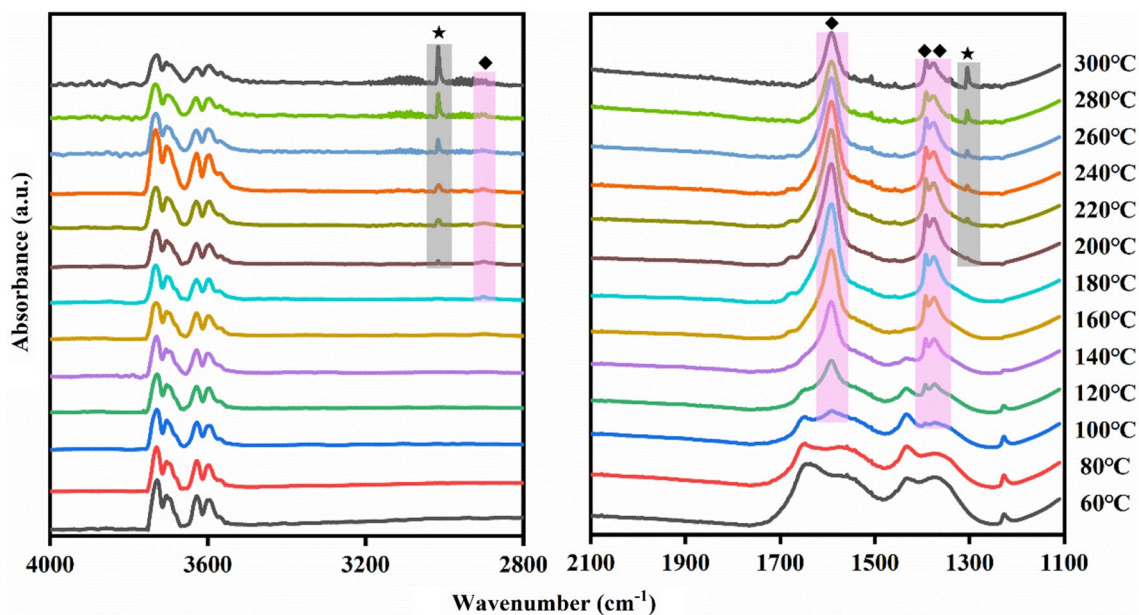|	Monodentate formate	Bidentate formate or bridged formate	Lineart CO on Ni	Nickel carbonyl hydride	Methane
$\Delta v = (v_{as}(O–C–O)-v_s(O–C–O))$	Larger than 220 cm^{-1}	close or less than 220 cm^{-1}			
V(C–O)			2019	1917	
$_v$(C–H)		2898			3016
δ(C–H)	1350	1372			1308

Fig. 9 In situ FTIR spectra of CO$_2$ methanation on Ni-Mn/γ-Al$_2$O$_3$ with a programmed temperature rise from 60 to 300 °C
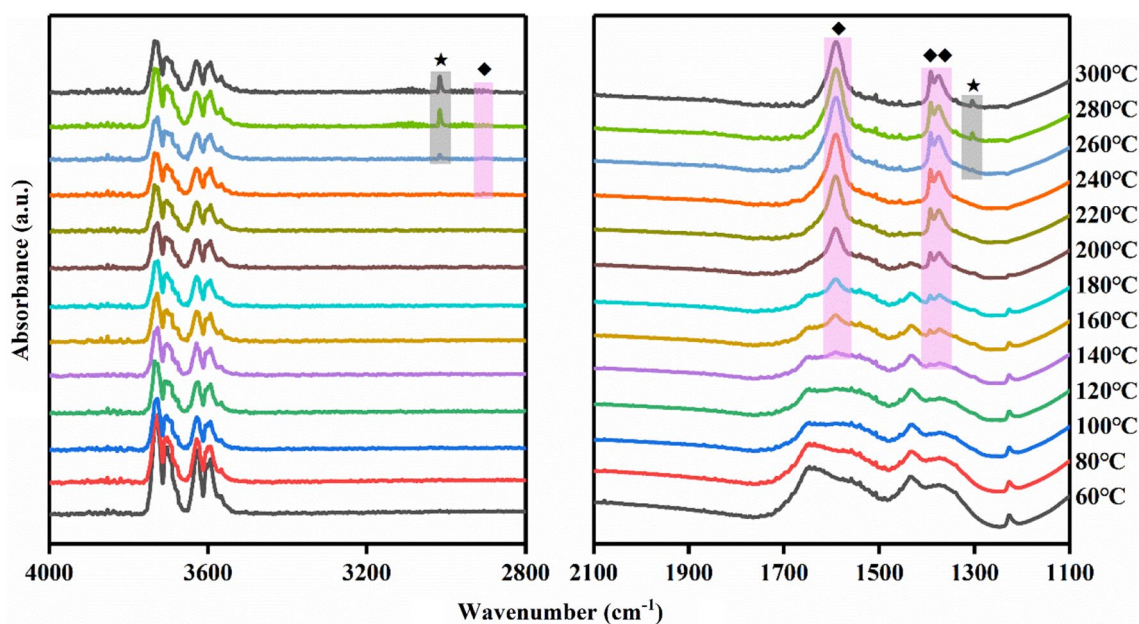

Fig. 10 In situ FTIR spectra of CO$_2$ methanation on Ni-Fe/γ-Al$_2$O$_3$ with a programmed temperature rise from 60 to 300 °C

made the active sites of carbonate more strongly basic (Fig. 12). As the temperature continued to rise, the peak corresponding to C–H stretching of formate was detected at 180 °C for Ni-Mn/γ-Al$_2$O$_3$ and at 220 °C for Ni-Fe/γ-Al$_2$O$_3$. The peaks corresponding to C–H stretching of CH$_4$ were observed at 200, 200, and 260 °C for Ni-Mn/γ-Al$_2$O$_3$, Ni-Co/γ-Al$_2$O$_3$, and Ni-Fe/γ-Al$_2$O$_3$, respectively. We presumed that the second metal interacts with Ni and

promotes its dispersion, which improves the ability of Ni to crack H* and cause it to overflow, thereby accelerating the process of H* spilling over from Ni to attack the C atom of formate. This process thereby improves the activity for CO$_2$ methanation. We also determined that the introduction of metal components enhances the activity in this order: Mn ≈ Co > Fe. It is also consistent with the catalyst activity test result wherein the addition of the
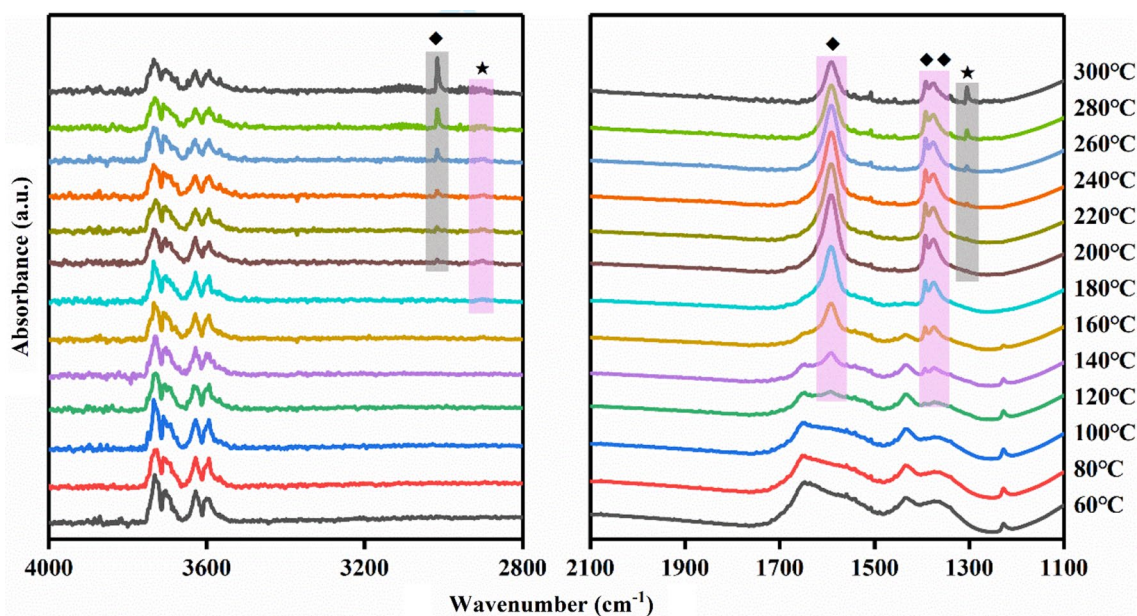
Fig. 11 In situ FTIR spectra of CO_2 methanation on Ni-Co/γ-Al$_2$O$_3$ with a programmed temperature rise from 60 to 300 °C

second metal (Fe, Co, or Mn) to Ni/γ-Al$_2$O$_3$ lowered the optimal reaction temperature of CO_2 methanation to varying degrees.

4 Conclusion

In summary, we successfully synthesised Ni-M/γ-Al$_2$O$_3$ (M=Co, Mn, or Fe) catalysts by an ultrasonic-assisted co-impregnation method. According to the in situ FTIR and

Fig. 12 CO_2 adsorption and methanation reaction mechanism diagram on catalysts

XPS measurements, the introduction of the second metal could increase the number of oxygen vacancies to strengthen the basicity of the O^{2-} sites, which is more conducive to the conversion of bicarbonate to carbonate. In addition, Mn and Co could significantly strengthen the hydrogenation ability of Ni to carbonate and formate, thereby lowering the methanation reaction activity temperature. In general, the mechanism and catalyst preparation strategy provide a feasible means to develop catalysts for CO_2 methanation at low temperatures.

Compliance with Ethical Standards

Conflict of interest The authors declare no conflict of interest.

References

1. Brewer PJ, Brown RJC, Miller MN, Minarro MD, Murugan A, Milton MJT, Rhoderick G (2014) Anal Chem 86:1887–1893
2. Vogt C, Monai M, Kramer GJ, Weckhuysen BM (2019) Nat Catal 2:188–197
3. Gao J-J, Wang Y-L, Ping Y, Xu D-C, Xu G-W, Gu F-N, Su F-B (2012) RSC Adv 2:2358–2368
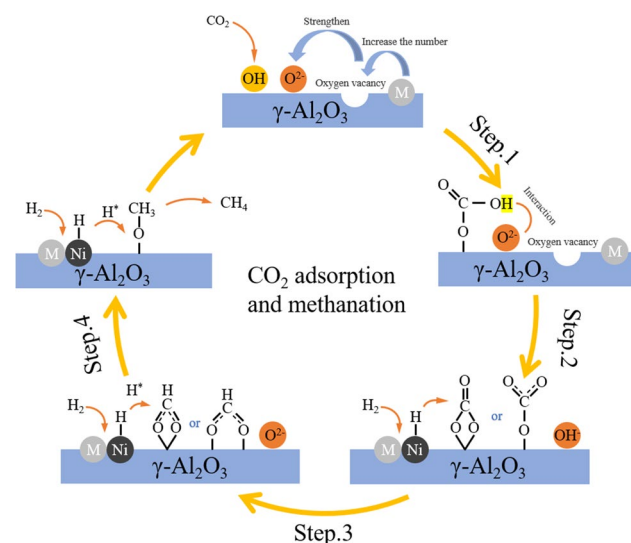4. Miguel CV, Soria MA, Mendes A, Madeira LM (2015) J Nat Gas Sci Eng 22:1–8

5. Wu Y-S, Lin J-H, Xu Y-F, Ma G-Y, Wang J, Ding M-Y (2020) Chem Cat Chem 12:3553–3559
6. Thampi KR, Lucarelli L, Kiwi J (1991) Langmuir 7:2642–2648
7. Karelovic A, Ruiz P (2013) ACS Catal 3:2799–2812
8. Ocampo F, Louis B, Roger A-C (2009) App Catal A 369:90–96
9. Kim HY, Lee HM, Park J-N (2010) Phys Chem C 114:7128–7131
10. Solymosi F, Erdohelyi A, Bansagi T (1981) J Catal 68:371–382
11. Huang Q-S, Lan L-Y, Wang A-J, Wang Y (2017) Petrochem Technol 46:1355–1360
12. Aziz MAA, Jalil AA, Triwahyono S, Ahmad A (2015) Cheminform 17:2647–2663
13. Shin HH, Lu L, Yang Z, Kiely CJ, Mcintosh S (2016) ACS Catal 6:2811–2818
14. Wang C-X, Gong J (2011) Nat Gas Chem Ind 36:4–6
15. Zhi G-J, Wang Y-Y, Jin G-Q (2016) Nat Gas Chem Ind 41:24–28
16. Vrijburg WL, Garbarino G, Chen W, Parastaev A, Hensen EJM (2020) J Catal 382:358–371
17. Li L-B, Wei S-Q, Xu G-L (2004) Nat Gas Chem Ind 29:27–31
18. Burger T, Wenng KA, Köhler TK, Hinrichsen O (2018) Catal Sci Technol 8:5920–5932
19. Serrer MA, Gaur A, Jelic J, Weber S, Fritsch C, Clark AH, Saraci E, Studt F, Grunwaldt JD (2020) Catal Sci Technol 10:7542–7554
20. Sandupatla AS, Banerjee A, Deo G (2019) App Surf Sci 485:441–449
21. Dreyer JAH, Li P-X, Zhang L-H, Beh GK, Zhang R-D, Sit PHL, Teoh WY (2017) App Catal B 219:715–726
22. Benitez JJ, Alvero R, Capitan MJ, Odriozola JA (1991) Appl Catal 71:219–231
23. Gupta NM, Kamble VS, Kartha VB (1994) J Catal 146:173–184
24. Eckle S, Denkwitz Y, Behm RJ (2010) J Catal 269:255–268
25. Marwood M, Doepper R, Renken A (1997) Appl Catal A 151:223–246
26. Lee WJ, Li C, Prajitno H, Yoo J, Patel J, Yang Y, Lim S (2020) Catal Today. https://doi.org/10.1016/j.cattod.2020.02.017
27. Burger T, Koschany F, Thomys O, Kohler K (2018) Appl Catal A 558:44–54
28. Burger T, Ewald S, Niederdrank A, Wagner FE, Kohler K, Hinrichsen O (2020) Appl Catal A 604:117778–117787
29. Zhao A-M, Ying W-Y, Zhang H-T, Ma H-F, Fang D-Y (2012) J Nat Gas Chem 21:17–177
30. Mutz B, Belimov M, Wu W, Sprenger P, Grunwaldt JD (2017) ACS Catal 7:6802–6814
31. Strohmeier BR, Hercules DM (1984) J Phys Chem 88:4922–4929
32. Lee KM, Lee WY (2002) Catal Lett 83:65–70
33. Hoffer BW, Langeveld ADV, Janssens JP, Bonne RLC, Lok CM, Moulijn JA (2000) Janssens Catal 192:432–440
34. Weidler N, Schuch J, Knaus F, Stenner P, Jaegermann W (2017) J Phys Chem C 121:6455–6463
35. Jian Z, Yang J, Bian ZF, Jie R, Liu YM, Yong C, Li HX, He HY, Fan KN (2007) Appl Catal B 76:82–91
36. He ZL, Que WX, Chen J, He CY, Wang GF (2013) J Phys Chem Solids 74:924–928
37. Lavalley JC (1996) Catal Today 27:377–401
38. Ewald S, Hinrichsen O (2019) Appl Catal A 580:71–80
39. Amenomiya Y, Morikawa Y, Pleizier G (1977) J Catal 46:431–433
40. Ewald S, Hinrichsen O (2019) Appl Catal A 580:7–80
41. Yu L, Song M, Williams PT, Wei Y (2019) Ind Eng Chem Res 58(27):11770–11778
42. Hasan M, Drazin J, Dey S, Castro RHR (2015) Am Miner 100:652–657
43. Matsuhashi H, Oikawa M, Arata K (2000) Langmuir 16:8201–8205
44. Kim HJ, Kang BS, Kim MJ, Park YM, Kim DK, Lee JS, Lee KY (2004) Catal Today 93–95:315–320
45. Hao E, Lian T (2000) Langmuir 16:7879–7881
46. Garbarino G, Bellotti D, Finocchio E, Magistri L, Busca G (2016) Catal Today 277:21–28
47. Lee SM, Lee YH, Moon DH, Ahn JY, Nguyen DD, Chang SW, Kim SS (2019) Ind Eng Chem Res 58:8656–8662
48. Baltrusaitis J, Jensen JH, Grassian VH (2006) J Phys Chem B 110:12005–12016
49. Bandara A, Kubota J, Wada A, Domen K, Hirose C (1996) J Phys Chem B 100:14962–14968
50. Collins SE, Baltanas MA, Bonivardi AL (2004) J Catal 226:410–421